Supporting Information

Bifunctional-Nano-Template Assisted Synthesis of Nanoporous $SrTiO_3$ Photocatalysts Toward Efficient Organic Pollutant Degradation

Shuxin Ouyang,[ab#*] Peng Li,[c#] Hua Xu,[ab] Hua Tong,[ab] Lequan Liu[c] and Jinhua Ye[abc*]

[a] TU-NIMS Joint Research Center and Tianjin Key Laboratory of Composite and Functional Materials, School of Material Science and Engineering, Tianjin University, P.R. China.
[b] Collaborative Innovation Center of Chemical Science and Engineering (Tianjin), Tianjin 300072, P.R. China.
[c] Environmental Remediation Materials Unit and International Center for Materials Nanoarchitectonics (WPI-MANA), National Institute for Materials Science (NIMS), Japan.
[#] These authors contributed equally.
[*] E-mail: oysx@tju.edu.cn; jinhua.ye@nims.go.jp

Table of Contents

SI-1 Details of Synthesis and Characterizations

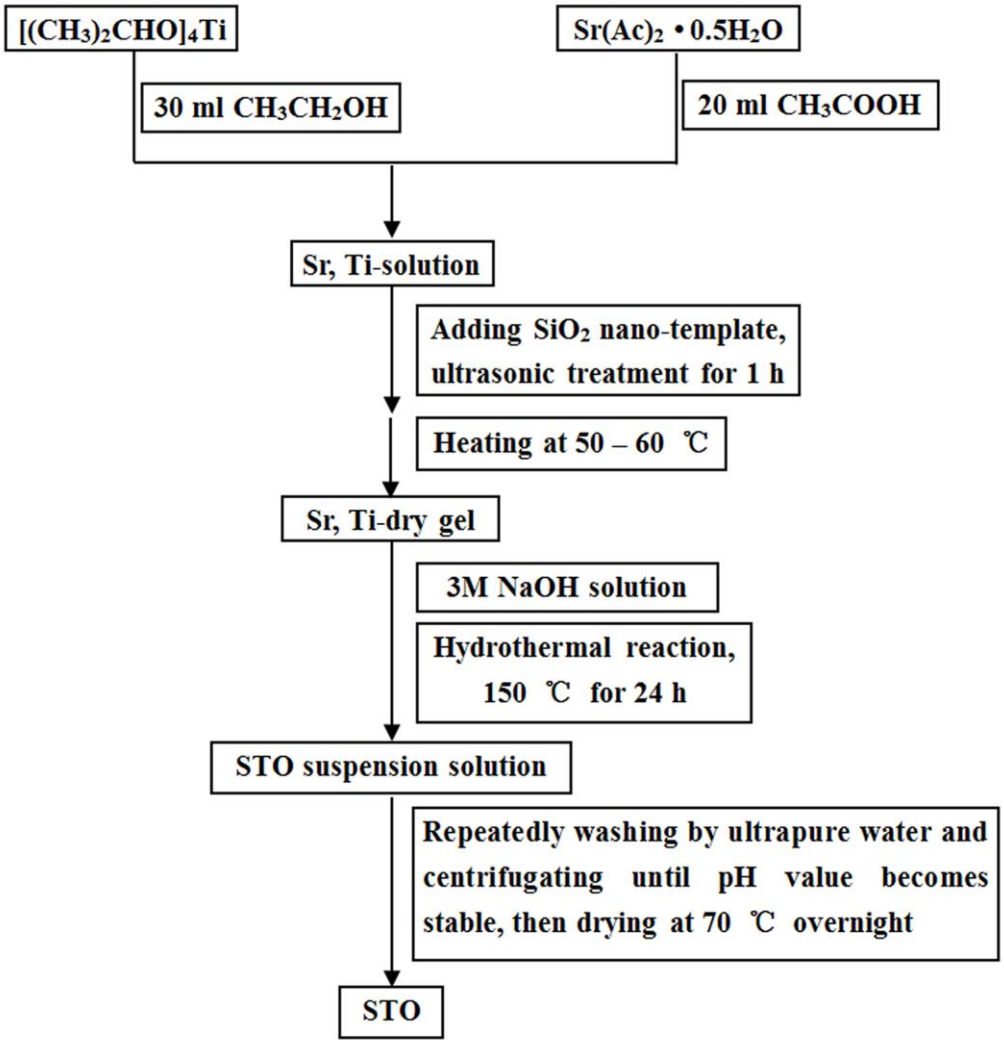

Figure S1. Synthetic flow chart of the micro-mesoporous $SrTiO_3$ photocatalyst.

Table S1. The synthesis details of other materials

Samples	Starting Materials [#,*]	Reaction Conditions
Cr doped $SrTiO_3$	0.05 mmol $Cr(NO_3)_3 \cdot 9H_2O$ 4.95 mmol $Sr(CH_3COO)_2 \cdot 0.5H_2O$ 5.00 mmol $[(CH_3)_2CHO]_4Ti$	3 M NaOH aqueous solution, 170 ^oC, 24 h
La,Cr codoped $SrTiO_3$	0.05 mmol $La(NO_3)_3 \cdot 6H_2O$ 0.05 mmol $Cr(NO_3)_3 \cdot 9H_2O$ 4.95 mmol $Sr(CH_3COO)_2 \cdot 0.5H_2O$ 4.95 mmol $[(CH_3)_2CHO]_4Ti$	3 M NaOH aqueous solution, 170 ^oC, 24 h
Li_2TiO_3	20 mmol CH_3COOLi 10 mmol $[(CH_3)_2CHO]_4Ti$	2 M NaOH + 1 M LiOH aqueous solution, 150 ^oC, 24 h
$Na_2Ti_3O_7$	10 mmol CH_3COONa 10 mmol $[(CH_3)_2CHO]_4Ti$	1 M NaOH aqueous solution, 150 ^oC, 24 h
$K_2Ti_4O_9$	10 mmol CH_3COOK 10 mmol $[(CH_3)_2CHO]_4Ti$	1 M KOH + 1 M K_2CO_3 aqueous solution, 150 ^oC, 24 h

[#] All the samples were added 40 wt% SiO_2 nano-template in the sol-gel process.

* The $Cr(NO_3)_3 \cdot 9H_2O$ and $La(NO_3)_3 \cdot 6H_2O$ were dissolved in ethylene glycol to prepare a certain concentration solutions in advance for precise doping. All the acetates were dissolved in glacial acetic acid and the $[(CH_3)_2CHO]_4Ti$ was dissolved in ethanol for the followed sol-gel process.

SI-2 Characterizations of SiO_2 Nano-template

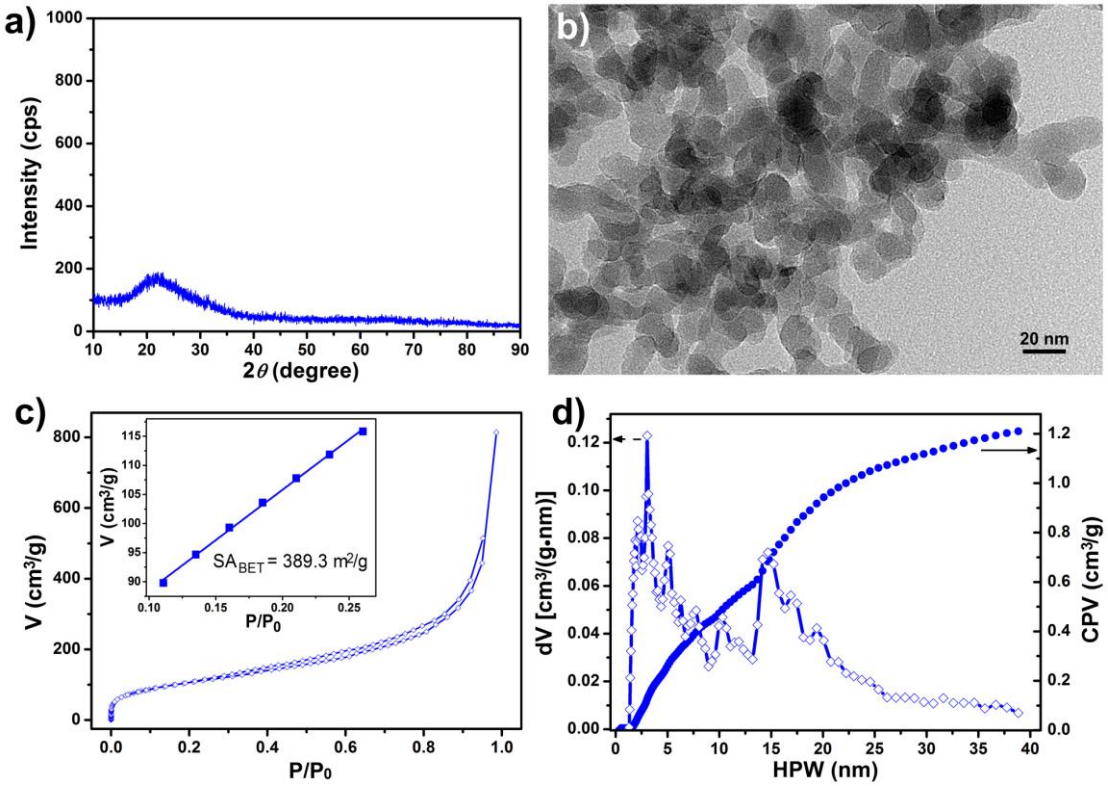

Figure S2. Characterizations of SiO_2 nano-template. (a) XRD pattern. (b) TEM image. (c) Nitrogen adsorption–desorption isotherms and linear part for BET surface area calculation (inset). (d) Pore distribution and cumulative pore volume analyzed by DFT simulation; HPW, half pore width; CPV, cumulative pore volume.

SI-3 Microstructural Feature and Chemical Compositions of Nanoporous $SrTiO_3$

Table S2. Pore types and distribution percentages

Samples	Micropore / % HPW < 1 nm	Mesopore I / % 1 nm < HPW < 10 nm	Mesopore II / % 10 nm < HPW
STO-SiO_2-10%	0	49.7	50.3
STO-SiO_2-20%	1.1	65.3	33.6
STO-SiO_2-30%	3.9	71.8	24.3
STO-SiO_2-40%	3.7	77.4	18.9
STO-SiO_2-50%	6.0	71.6	22.4
STO-SiO_2-60%	5.6	75.4	19.0
STO-SiO_2-70%	7.2	73.4	19.4
STO-SiO_2-80%	8.8	73.6	17.6
STO-SiO_2-90%	5.7	60.9	33.4

Table S3. Chemical Compositions of as-prepared $SrTiO_3$ samples

Samples	Elements / wt%[#]			Molar Ratio of Sr : Ti
	Sr	Ti	Si	
STO-SiO_2-10%	41.2	22.6	1.90	0.996 : 1.000
STO-SiO_2-30%	40.0	21.8	3.08	1.002 : 1.000
STO-SiO_2-50%	38.9	21.2	3.95	1.002 : 1.000
STO-SiO_2-90%	37.0	19.8	5.08	1.007 : 1.000

[#] The weight percentages of elements were measured by ICP-OES.

SI-4 Calculation of FWHM in XRD Pattern

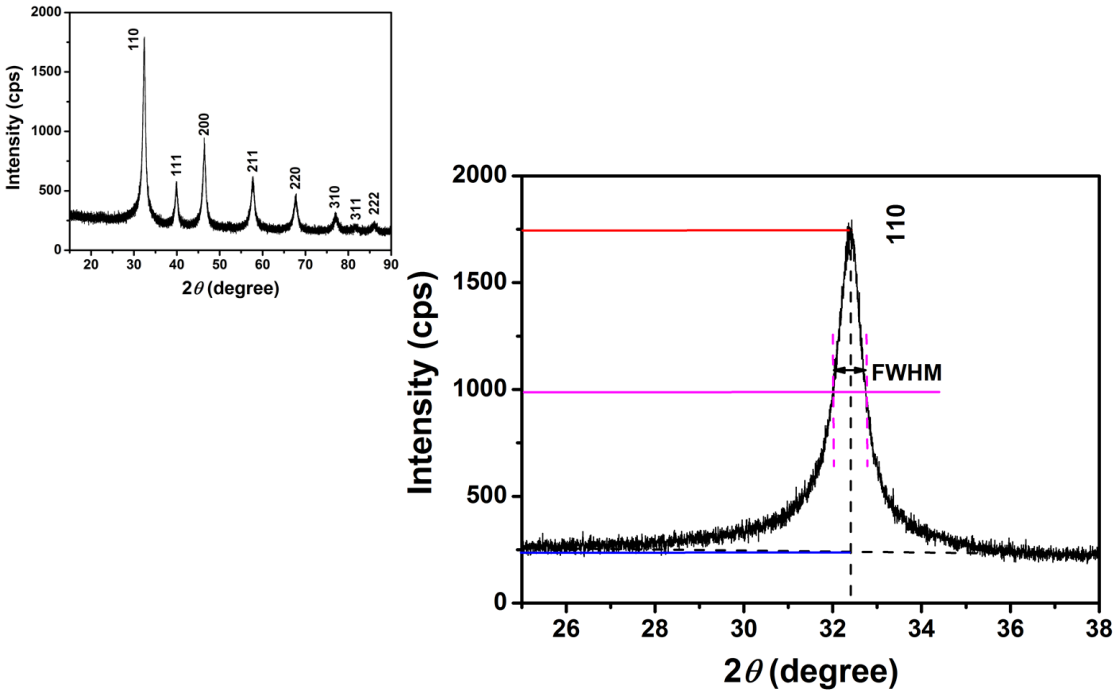

Figure S3. XRD patterns of STO-SiO_2-30%.

Taking the STO-SiO_2-30% sample as an example to introduce the calculation of the FWHM in the XRD pattern,

for all the $SrTiO_3$ samples in this study, we took the (110) peak as an index peak;

firstly, enlarging the (110) peak of XRD pattern, then marking the peak center and background as shown by the black dash lines;

secondly, recording the peak intensity, I_{peak}, as presented by the red line, then recording the background intensity (the crossing point of two black dash lines), $I_{background}$ as presented by the blue line;

thirdly, calculating the intensity of the half maximum, $I_{hm} = (I_{peak} - I_{background})/2 + I_{background} = (1762 – 231)/2 +231 = 997$;

finally, marking the height of the half maximum (as shown by the magenta line) and measuring the FWHM = 0.720 °.

SI-5 Influence of SiO_2 Nano-template on Crystallization

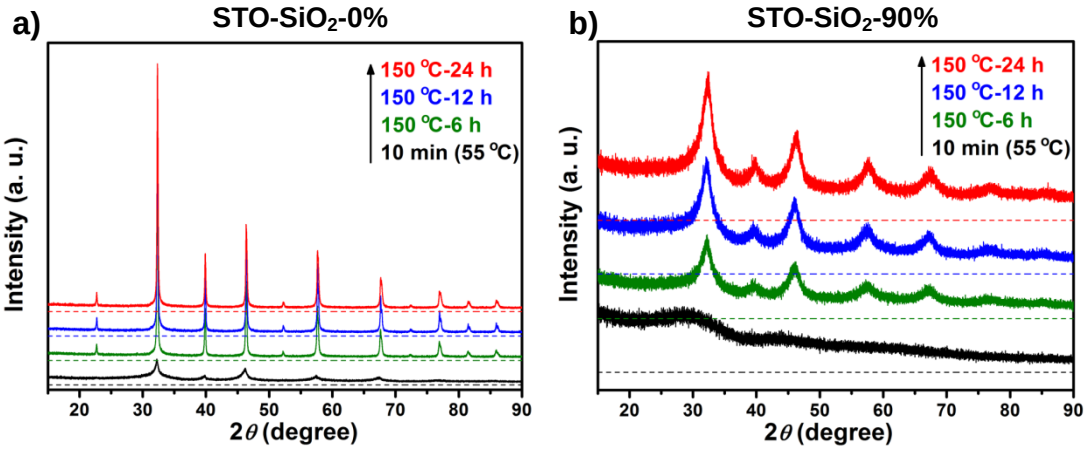

Figure S4. XRD patterns of $SrTiO_3$ samples without (a) and with (b) SiO_2 nano-template in synthesis. The dash lines are the baselines of each samples, where absolute intensities = 0

Table S4. Crystallinity variation of $SrTiO_3$ samples without and with SiO_2 nano-template in synthesis under different reaction times.

Reaction Time	*FWHM* of STO-SiO_2-0% / °	*FWHM* of STO-SiO_2-90% / °
10 min (55 °C)[#]	0.66	(amorphous)
150 °C 6 h	0.19	1.98
150 °C 12 h	0.18	2.04
150 °C 24 h	0.18	1.84

[#]Before hydrothermal reaction, after adding NaOH (12 g) into the STO-gel suspension solution (100 mL), the highest temperature of solution reached 55 °C.

A contrast study of the reaction-time-dependent crystallinity variation between the STO-SiO_2-0% and STO-SiO_2-90% samples was carried out (Figure S4 and Table S4). According to the value change of FWHM, the sample without nano-template (STO-SiO_2-0%) could crystallize quickly and reach growth equilibrium after 12 h hydrothermal treatment; in contrast, the sample with 90% nano-template (STO-SiO_2-90%) underwent a very slow growing during the whole synthesis process. Thereby, it was found that the SiO_2 nano-template dominated the crystallization rate of $SrTiO_3$.

Table S5. Conversion percentages of Si element from the SiO_2 to the Na_2SiO_3 under different reaction times

Reaction Time	CP_{HRS} [#] / %	*TCP** / %
0 min [#]	0.0	-
10 min (55 °C)*	31.9	-
150 °C 2 h	60.1	-
150 °C 6 h	60.5	-
150 °C 12 h	63.1	-
150 °C 24 h	67.5	76.2

[#] CP_{HRS}, conversion percentage in hydrothermal reaction solution. The hydrothermal reaction solution was measured the Si concentration ($[Si]_{HRS}$) by ICP-AES. The CP_{HRS} = $[Si]_{HRS} * V_{HRS} / m(Si)_{template} * 100\%$.

* *TCP*, total conversion percentage. After hydrothermal reaction and separating samples from hydrothermal reaction solution, the samples were treated by ultrasonic-cleaning with ultrapure water and centrifugally separated. The solutions that contained the Na_2SiO_3 desorbed from the sample surface were collected and mixed with the hydrothermal reaction solution, and then the mixed solution was concentrated and measured the Si concentration ($[Si]_{HRS+OSS}$) by ICP-AES. The *TCP* = $[Si]_{HRS+OSS} * V_{concentrated} / m(Si)_{template} * 100\%$.

In NaOH aqueous solution, the SiO_2 reacts with NaOH to form Na_2SiO_3, and then the Na_2SiO_3 can dissolve into water. The conversion of Si element from SiO_2 to Na_2SiO_3 in the present synthesis can be detected via the inductance coupling plasma-optical emissive spectrum (ICP-OES) measurement for the reaction solution (Table S5). For the STO-SiO_2-90% sample, at initial stage of synthesis (after adding NaOH into the precursor suspension solution and during beginning of the hydrothermal reaction), the conversion percentage of Si element from SiO_2 to Na_2SiO_3 in hydrothermal reaction solution, CP_{HRS}, rapidly increased from 0% to 60.1%, because the big organic frame of precursor deconstructed into a large amount of sub-micro particles (tens to hundreds of nanometers in size) and released a lot of SiO_2 into solution. The process was accompanied with the formation of a huge number of tiny crystal nucleuses. However, the remnant SiO_2 nano-templates in the sub-micro particles dissolved to generate Na_2SiO_3 and then dispersed from the inner of pores and the surface into solution very slowly, which could be supported by the evidence that the CP_{HRS} slightly increased from 60.1% to 67.5% during 2 h to 24 h of hydrothermal reaction. Furthermore, when we cleaned the STO-SiO_2-90% sample under 24 h hydrothermal treatment carefully, and then collected the hydrothermal solution and all the cleaning solution to measured ICP-OES for calculating the total conversion percentage of Si element from SiO_2 to Na_2SiO_3, *TCP* (Table S5). It reached 76.2% which was obviously higher than the CP_{HRS}, indicating that the slow increase of Si element in hydrothermal solution with increasing the reaction time indeed resulted from the slow release of Na_2SiO_3 from the surface and inner of $SrTiO_3$ particle.

SI-6 Characterizations of Commercial Nano-$SrTiO_3$

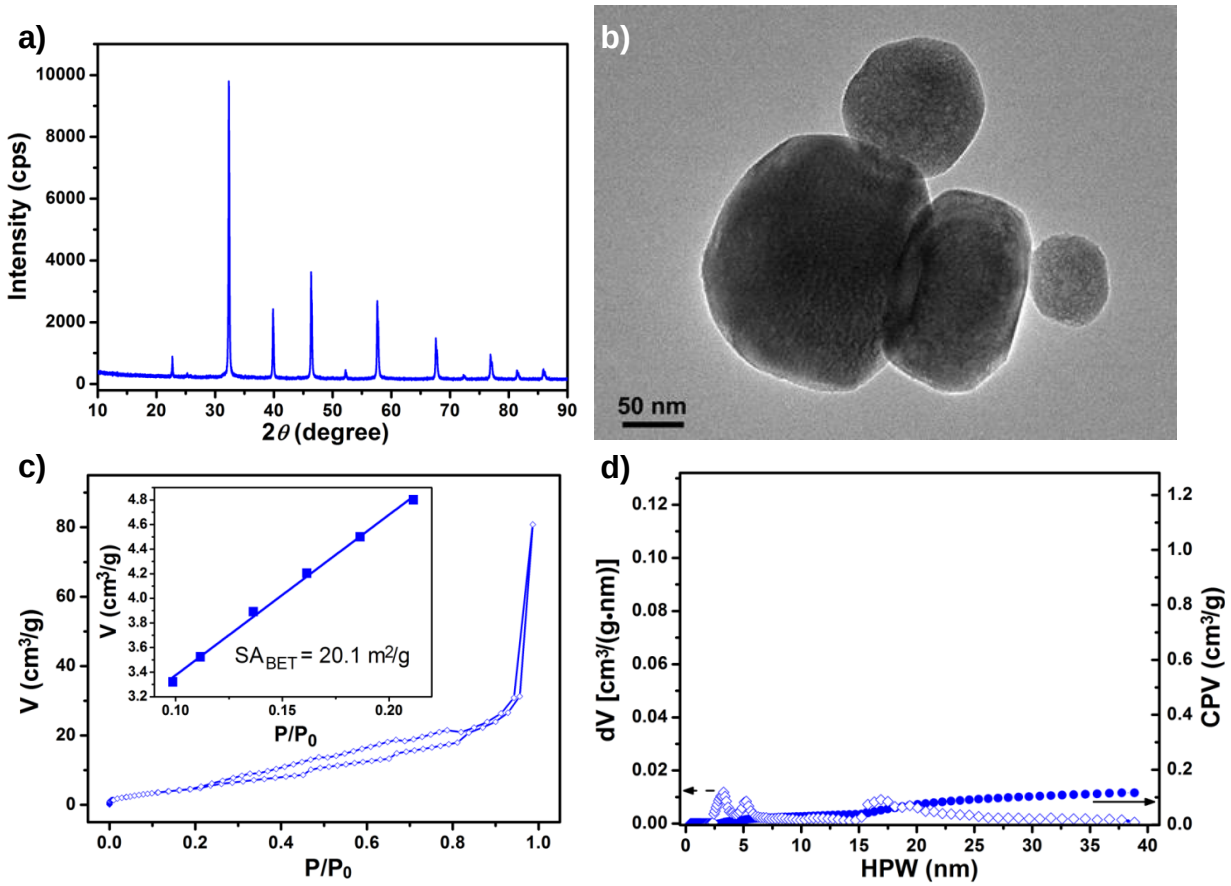

Figure S5. Characterization of commercial nano-sized $SrTiO_3$ (C-Nano-STO for short; No.329-43442, Wako, Japan). (a) XRD pattern. (b) TEM image. (c) Nitrogen adsorption–desorption isotherms and linear part for BET surface area calculation (inset). (d) Pore distribution and cumulative pore volume analyzed by DFT simulation; HPW, half pore width; CPV, cumulative pore volume.

SI-7 More Detailed Data of Photocatalytic Characterizations

IPA photodegradation over different STO samples

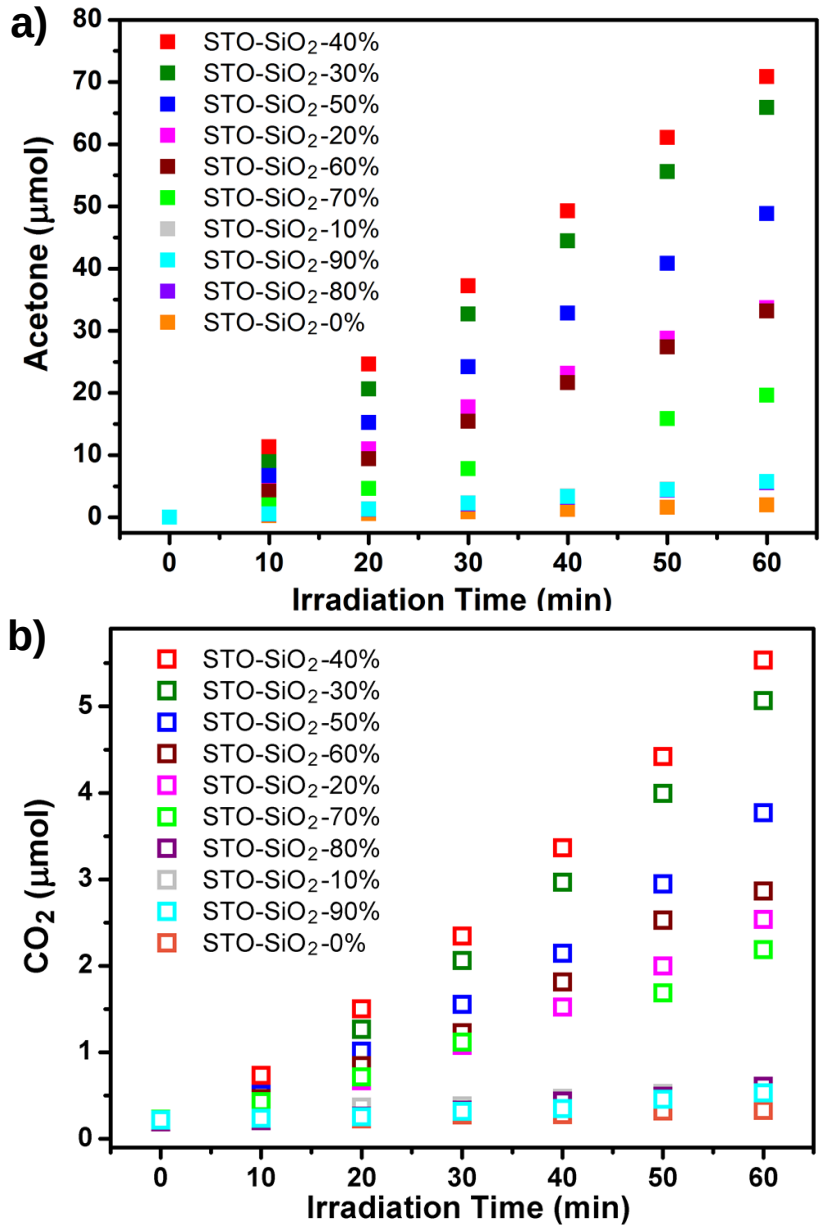

Figure S6. Acetone (a) and CO_2 (b) evolution amounts over different $SrTiO_3$ samples under UV-visible light irradiation (λ > 300 nm) as a function of irradiation time.

Stability test of IPA photodegradation over STO-SiO_2-40%

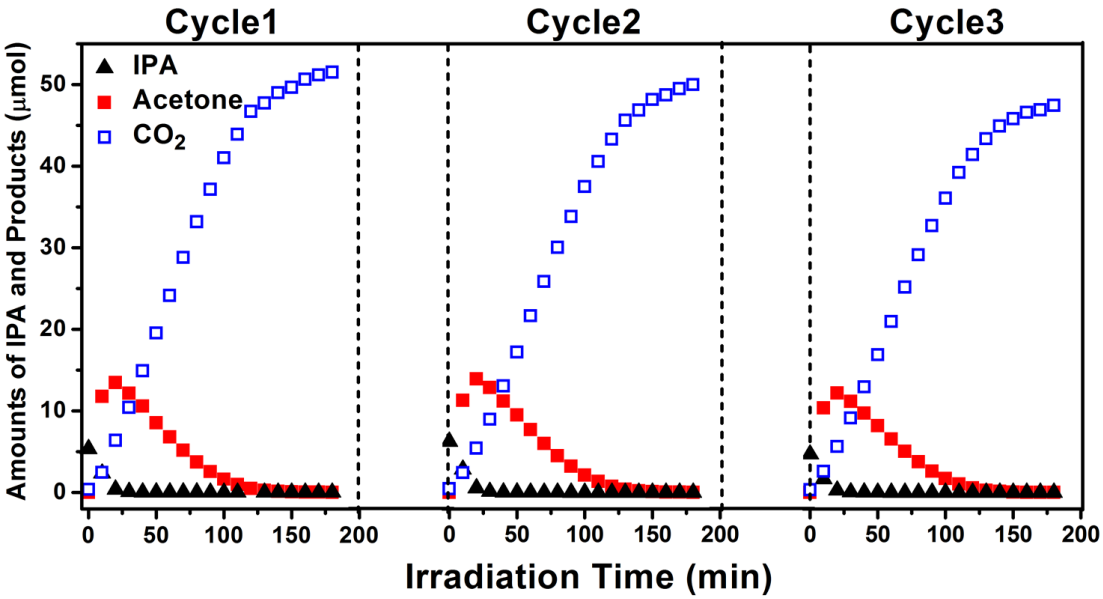

Figure S7. Cycle experiments of IPA photodegradation over STO-SiO_2-40% under UV-visible light irradiation (λ > 300 nm) with an irradiation period of 180 min.

SI-8 Characterizations of Nanoporous Doped $SrTiO_3$

To exemplify our synthetic process is available in the case of doped $SrTiO_3$, we fabricated the Cr doped $SrTiO_3$ (Cr is doped into the Sr site of $SrTiO_3$) and La, Cr codoped $SrTiO_3$ (La and Cr are doped into the Sr and Ti sites of $SrTiO_3$, respectively). The detailed synthetic conditions are listed in Table S1.

The doped $SrTiO_3$ samples crystallize in the same symmetry as the undoped $SrTiO_3$ (Figure S8a) but extend their light absorption into visible region (Figure S8b). The hysteresis loops in the N_2 adsorption-desorption isotherms (Figure S9a, S10a) indicate that the porous structures exist in both Cr doped $SrTiO_3$ and La, Cr codoped $SrTiO_3$. Similar to the undoped $SrTiO_3$, the major pores in these samples are also HPW < 10 nm. However, the codoped material has more uniform pore than the mono-doped case (Figure S9b, S10b). Both they contain a little amount of micropore with a main size of 2 – 5 Å (Figure S9c, S10c). These doped samples are nanocrystal-constructed microspheres with average diameters of about 200 and 400 nm for Cr doped $SrTiO_3$ and La, Cr codoped $SrTiO_3$, respectively (Figure S9d,e, S10d,e). The resolved lattice fringes observed from the edges of microspheres indicate the samples are crystallized (Figure S9f, S10f).

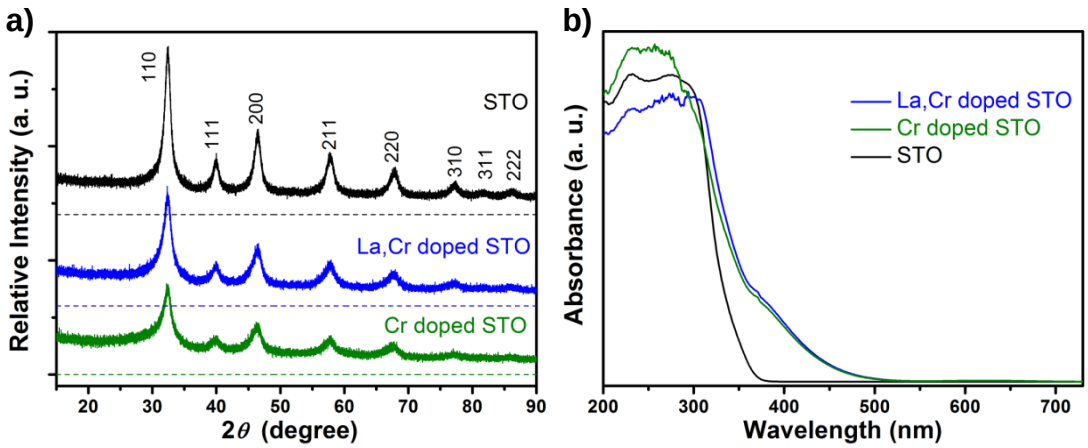

Figure S8. XRD patterns (a) and UV-visible absorption spectra (b) of $SrTiO_3$, Cr doped $SrTiO_3$, and La,Cr doped $SrTiO_3$. (The $SrTiO_3$ reference sample was synthesized under the similar conditions of doped $SrTiO_3$ samples; 40% SiO_2 nano-template, 3 M NaOH, 170 ^oC, 24 h.)

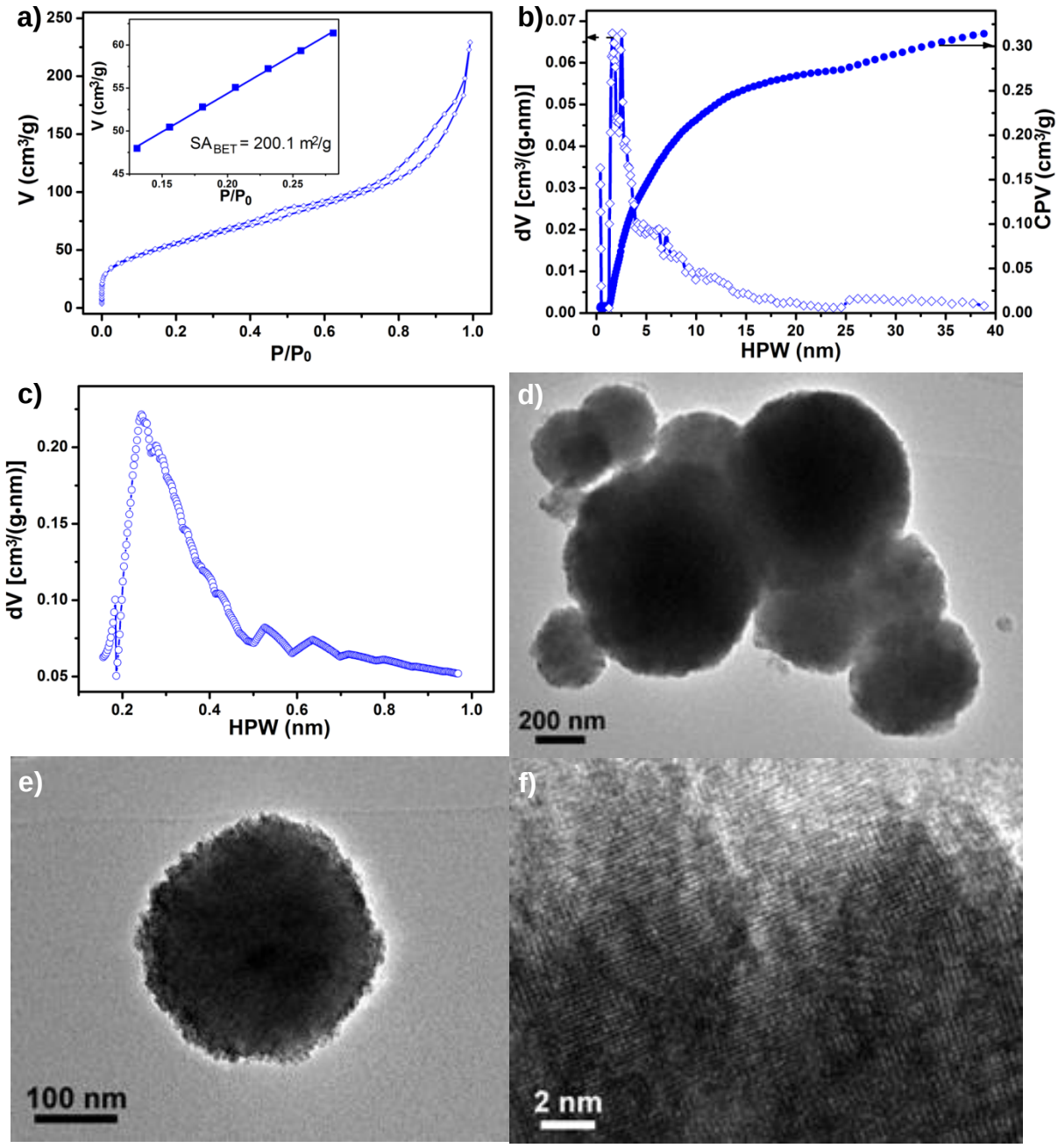

Figure S9. Pore and morphology characterizations for the Cr doped $SrTiO_3$ sample. (a) Nitrogen adsorption–desorption isotherms and linear part for BET surface area calculation (inset). (b,c) Pore distribution and cumulative pore volume analyzed by DFT (for micropore and mesopore) and HK (for micropore only) simulation; HPW, half pore width; CPV, cumulative pore volume. (d,e) TEM images. (f) HRTEM image.

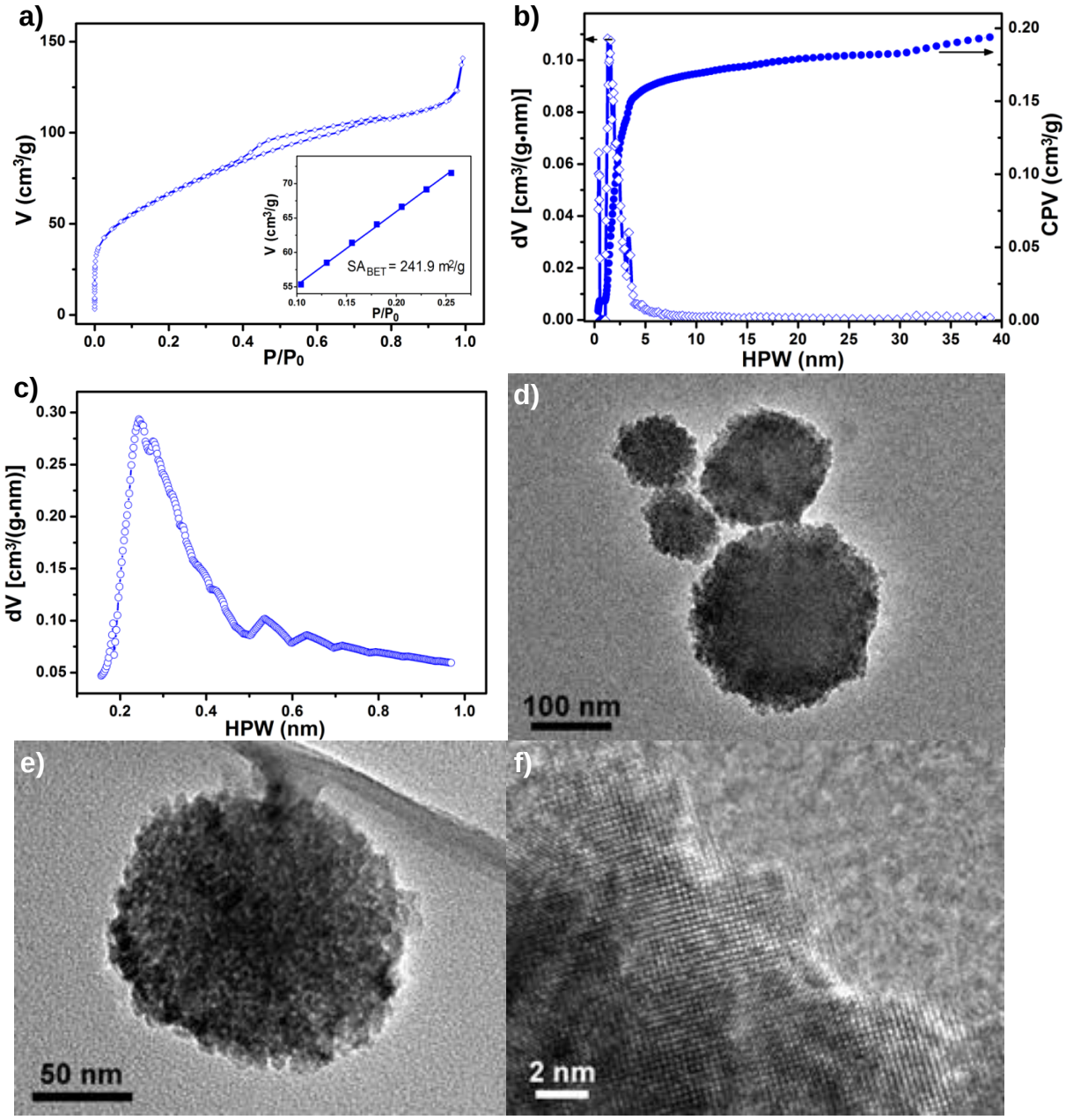

Figure S10. Pore and morphology characterizations for the La,Cr doped $SrTiO_3$ sample. (a) Nitrogen adsorption–desorption isotherms and linear part for BET surface area calculation (inset). (b,c) Pore distribution and cumulative pore volume analyzed by DFT (for micropore and mesopore) and HK (for micropore only) simulation; HPW, half pore width; CPV, cumulative pore volume. (d,e) TEM images. (f) HRTEM image.

SI-9 Characterizations of Nanoporous Alkali-metal Titanates

To exemplify our synthetic process is applicable for the alkali-metal titanates, we synthesized three typical materials, such as Li_2TiO_3, $Na_2Ti_3O_7$, and $K_2Ti_4O_9$. The detailed synthetic conditions are listed in Table S1.

The Li_2TiO_3 grows in a monoclinic symmetry (Figure S11a). The N_2 adsorption-desorption isotherm shows a typical hysteresis loop (Figure S11b), indicating this material possesses the porous structure. The HPW of these pores mainly distributes below 10 nm, but the micro-pore structure is not detected (Figure S11c). The BET surface area of this sample reaches 215.2 m^2/g. The TEM images present that this material are irregular particles which are loosely aggregated by a number of nanocrystals (Figure S11d), and thus some of these nanocrystals easily depart from the assembled particle to form monodispersed status (Figure S11e-f).

The $Na_2Ti_3O_7$ also crystallizes in a monoclinic symmetry (Figure S12a). A typical hysteresis-loop figure in the N_2 adsorption-desorption isotherm reveals the sample contains porous structure (Figure S12b). The material shows highly uniform pore-size distribution, and the HPW of the major pores is smaller than 5 nm, but the micro-pore structure is not observed (Figure S12c). The TEM images exhibit that this material are irregular particles with size from several hundred nanometers to several micrometers (Figure S12d).

The $K_2Ti_4O_9$ grows as a monoclinic-phase structure (Figure S13a). The contained porous structure can be revealed by the typical hysteresis loop in the N_2 adsorption-desorption isotherm (Figure S13b). This material also presents highly uniform pore size; the HPW mainly distributes below 5 nm (Figure S13c), and the micro-pore structure with a major HPW between 2 and 4 Å is detected (Figure S13d). The TEM images indicates that the sample is some aggregates of layered nanocrystals (Figure S13e,f; blue arrows mark the layered micro-structures); the particle size is from several hundred nanometers to several micrometers.

1. Li_2TiO_3

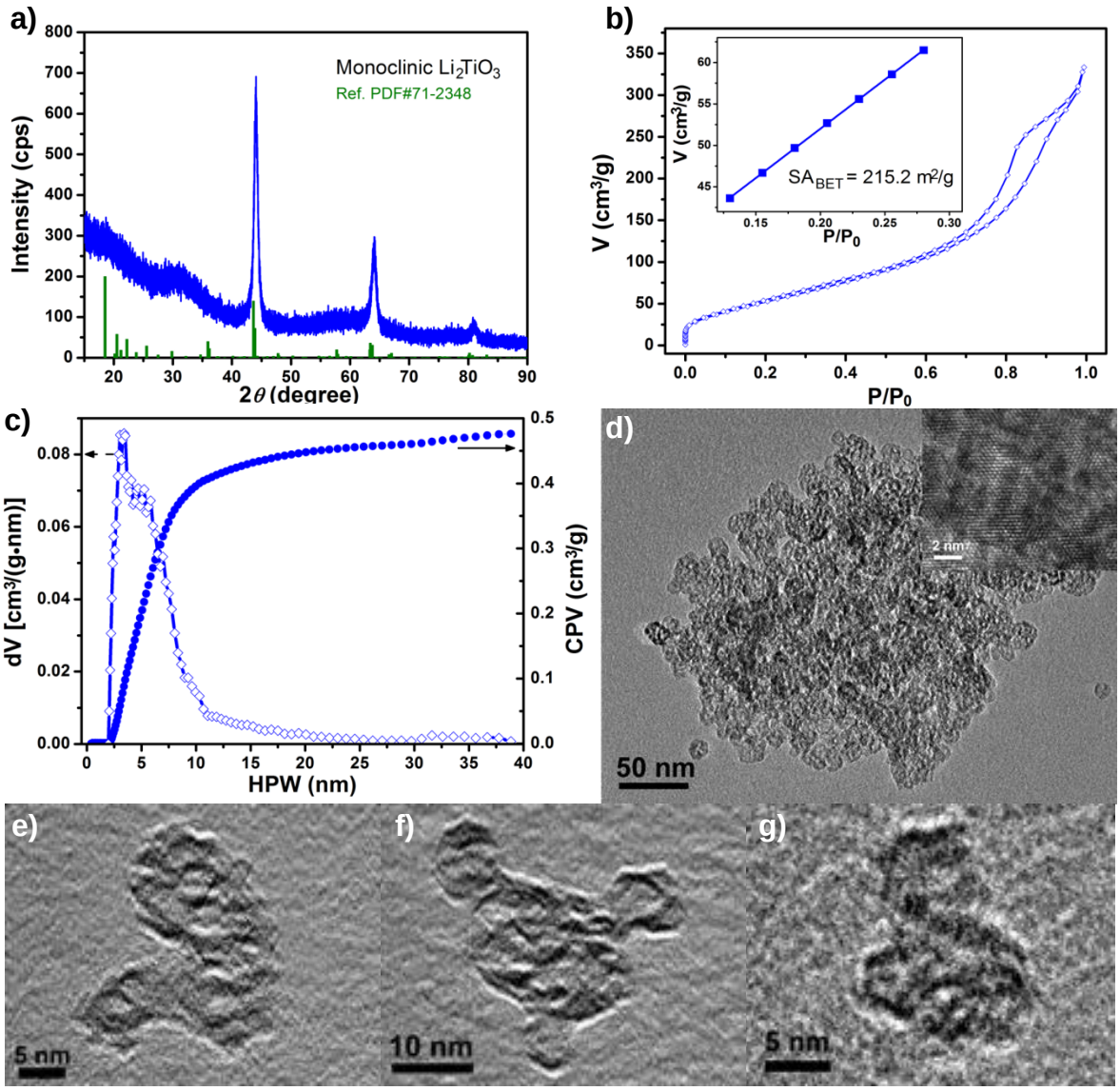

Figure S11. Crystal structure, pore and morphology characterizations for the Li_2TiO_3 sample. (a) XRD pattern. (b) Nitrogen adsorption–desorption isotherms and linear part for BET surface area calculation (inset). (c) Pore distribution and cumulative pore volume analyzed by DFT simulation; HPW, half pore width; CPV, cumulative pore volume. (d~g) TEM images and (d, inset) HRTEM image.

2. $Na_2Ti_3O_7$

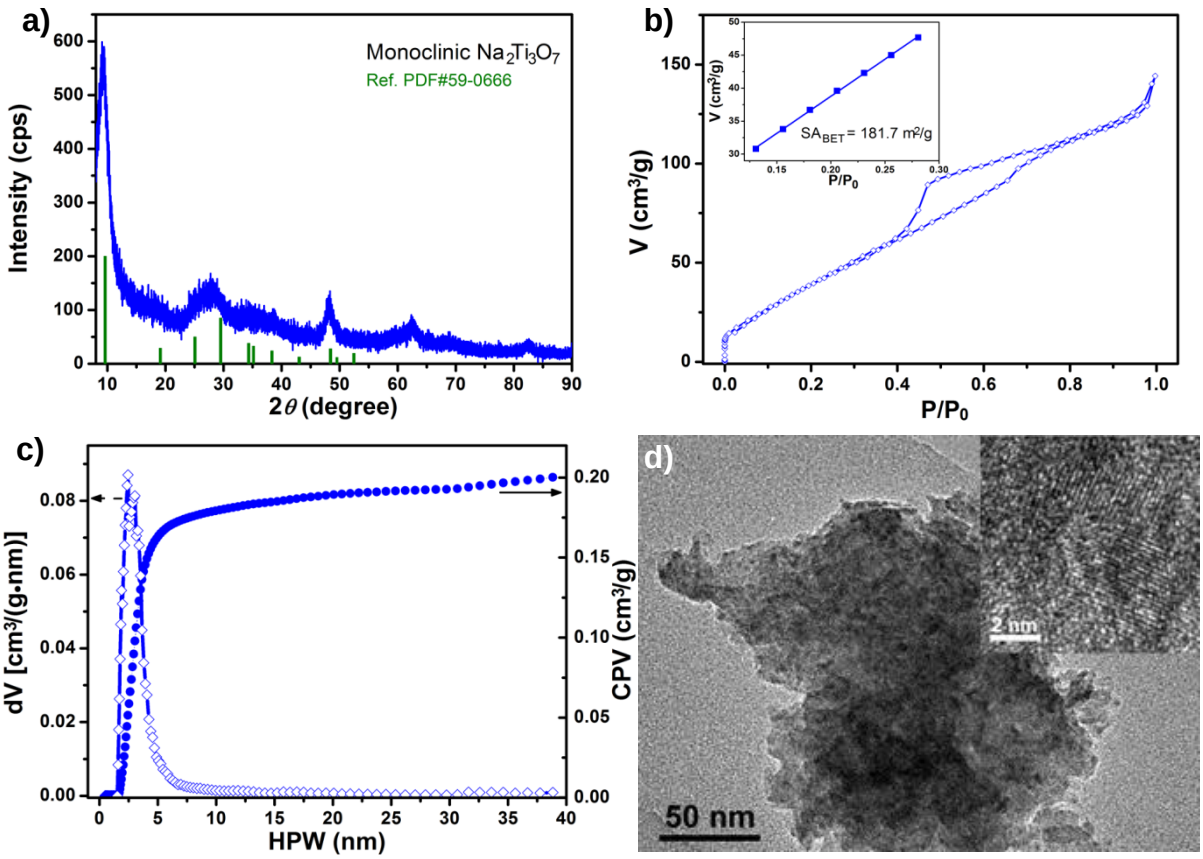

Figure S12. Crystal structure, pore and morphology characterizations for the $Na_2Ti_3O_7$ sample. (a) XRD pattern. (b) Nitrogen adsorption–desorption isotherms and linear part for BET surface area calculation (inset). (c) Pore distribution and cumulative pore volume analyzed by DFT simulation; HPW, half pore width; CPV, cumulative pore volume. (d) TEM and HRTEM (inset) images.

3. $K_2Ti_4O_9$

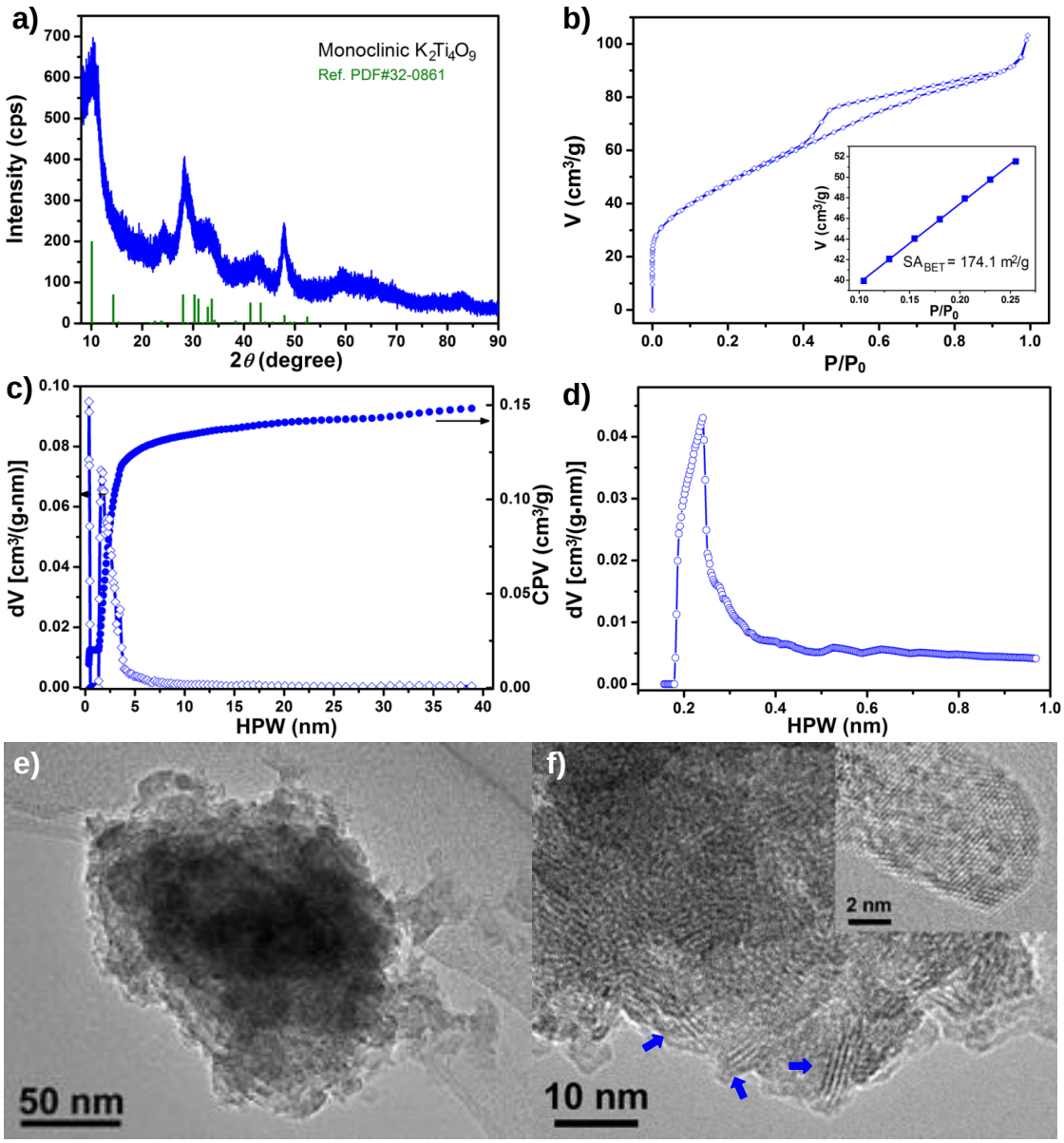

Figure S13. Crystal structure, pore and morphology characterizations for the $K_2Ti_4O_9$ sample. (a) XRD pattern. (b) Nitrogen adsorption–desorption isotherms and linear part for BET surface area calculation (inset). (c,d) Pore distribution and cumulative pore volume analyzed by DFT (for micropore and mesopore) and HK (for micropore only) simulation; HPW, half pore width; CPV, cumulative pore volume. (e,f) TEM and HRTEM (f, inset) images.